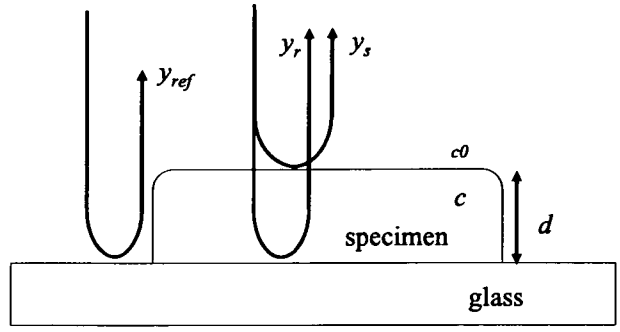

Fig. 2. Schematic illustration of reflections. y_{ref}: reflection from glass, y_r: reflection from the interface between glass and tissue, y_s: reflection from tissue surface.

same position for each of the sixteen frames. The attenuation was then determined from the amplitude and thickness, and the sound speed was determined from the phase shift and thickness.

Figure 2 shows a schematic of pulse propagation in water, tissue, and glass surface. Equation (1) shows the relationship between the frequency, amplitude, and phase due to interference between the reflections from the upper and lower surfaces of the specimen.

$$\begin{aligned} y_r &= y_s + y_b \\ &= e^{-(\alpha + j\frac{2\pi f}{c})d} \\ &= e^{-j\frac{2\pi f}{c}d} \cdot e^{-A_0 f^n d} \end{aligned} \tag{1}$$

where y_r is the received signal, y_s is the signal reflected from the surface of the specimen, y_b is the signal reflected from the interface between the tissue and glass, f is the frequency, c is the sound speed of the specimen, and d is the thickness of the specimen. The thickness was calculated at six regions in an image. The average value of thickness was applied to all pixels for calculation of attenuation and sound speed.

2.3. Sound speed scanning acoustic microscopy

Figure 3 shows a block diagram of sound speed microscopy for biological tissue characterization. A single ultrasound pulse with a pulse width of 5 ns was emitted and received by the same transducer above the specimen. The aperture diameter of the transducer was 1.2 mm, and the focal length was 1.5 mm. The central frequency was 80 MHz, and the pulse repetition rate was 10 kHz. The diameter of the focal spot was estimated to be 20 μm at 80 MHz by taking into account the focal distance and sectional area of the transducer. Distilled water was used as the coupling medium between the transducer and the specimen. The reflections from the tissue surface and those from the interface between the tissue and glass were received by the transducer and were introduced into a digital oscilloscope (Tektronics TDS 5052, USA). The frequency range was 300 MHz, and the sampling rate was 2.5 GS/s. Four values of the time taken for a pulse response at the same point were averaged in the oscilloscope in order to reduce random noise.

The transducer was mounted on an X-Y stage with a microcomputer board that was driven by the computer installed in the digital oscilloscope through RS232C. The X-scan was driven by a linear servo motor, and the Y-scan was driven by a stepping motor. Finally, two-dimensional distributions of ultrasonic intensity, sound speed, and thickness of a specimen measuring 2.4 × 2.4 mm were visualized using 300 × 300 pixels. The total scanning time was 121 s.

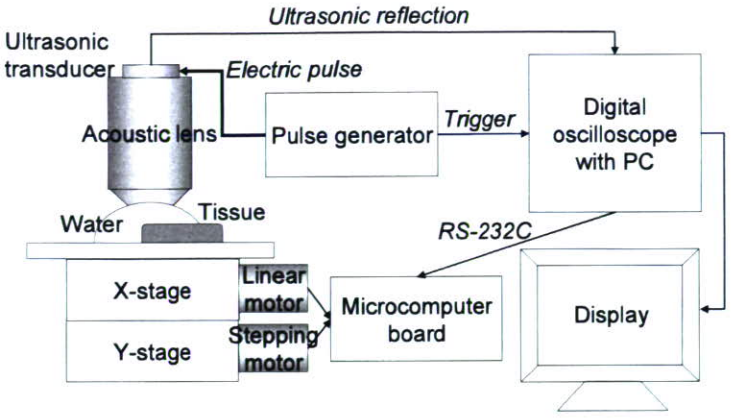

Fig. 3. Block diagram of sound speed scanning acoustic microscopy developed with collaboration between Tohoku University, Toyohashi University of Technology and Honda Electronics Co. Ltd. in 2003.

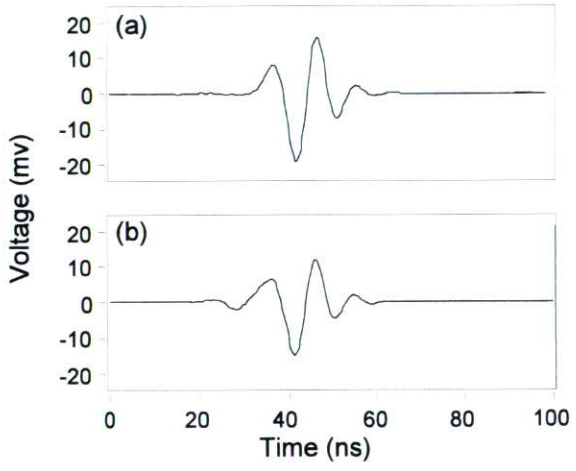

Fig. 4. Reflected waveforms (a) from the glass surface without tissue, and (b) from the tissue area.

2.4. *Signal analysis [10]*

The reflected waveforms are shown in Fig. 4. The waveform at the glass surface without the tissue is shown in (a). This signal was used as a reference waveform. The decline of the glass surface was compensated by measuring three different points in the glass area surrounding the tissue. The waveform from the tissue area is shown in (b). Although the waveform contains two reflections at the surface and at the interface of the tissue and glass, the two components cannot be separated in time domain analysis. Thus, frequency domain analysis was performed by analyzing the interference between the two reflections. Intensity and phase spectra were calculated by Fourier transforming the waveform. The spectra were normalized by the reference waveform. Figure 5 shows the frequency domain analysis of the interfered waveform.

Denoting the minimum point in the intensity spectrum by $f_{\min}$ and the corresponding phase angle by

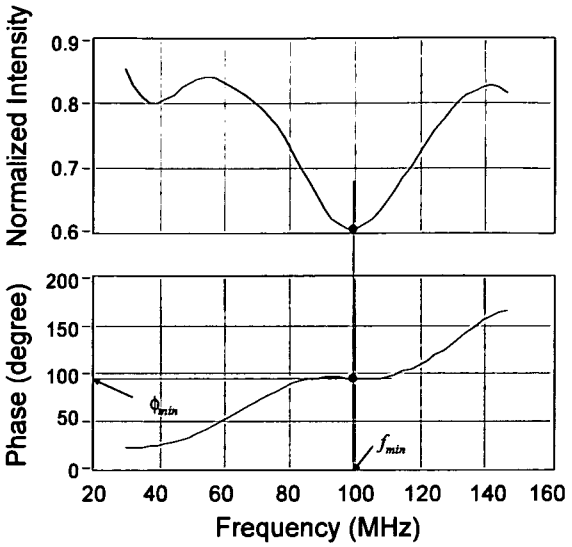

Fig. 5. Frequency domain analysis of interfered waveform. $f_{\min}$: the minimum point in the intensity spectrum, $\phi_{\min}$: corresponding phase angle.

$\phi_{\min}$, the phase difference between the two reflections at the minimum point is $(2n-1)\pi$, which yields

$$2\pi \boldsymbol{f}_{\min} \times \frac{2\boldsymbol{d}}{c_0} = \phi_{\min} + (2\boldsymbol{n}-1)\pi \tag{2}$$

where $\boldsymbol{d}$, c_0, and $\boldsymbol{n}$ are the tissue thickness, sound speed of water, and a non-negative integer, respectively. Denoting the maximum point in the intensity spectrum by $\boldsymbol{f}_{\max}$ and the corresponding phase angle by $\phi_{\max}$, the phase difference at the maximum point is $2n\pi$, which yields

$$2\pi \boldsymbol{f}_{\max} \times \frac{2\boldsymbol{d}}{c_0} = \phi_{\max} + 2\boldsymbol{n}\pi \tag{3}$$

The phase angles $\phi_{\min}$ and $\phi_{\max}$ can be expressed by

$$2\pi \boldsymbol{f}_{\min} \times 2\boldsymbol{d}\left(\frac{1}{c_0} - \frac{1}{c}\right) = \phi_{\min} \tag{4}$$

$$2\pi \boldsymbol{f}_{\max} \times 2\boldsymbol{d}\left(\frac{1}{c_0} - \frac{1}{c}\right) = \phi_{\max} \tag{5}$$

since $\phi_{\min}$ or $\phi_{\max}$ is the phase difference between the wave that travels the distance $2\boldsymbol{d}$ with sound speed c and the wave that travels a corresponding distance with sound speed $\boldsymbol{c}_0$. By solving Eqs (2) and (4),

$$\boldsymbol{d} = \frac{\boldsymbol{c}_0}{4\pi \boldsymbol{f}_{\min}}\{\phi_{\min} + (2\boldsymbol{n}-1)\pi\} \tag{6}$$

is obtained for the minimum point. Solving Eqs (3) and (5) yields

$$\boldsymbol{d} = \frac{\boldsymbol{c}_0}{4\pi \boldsymbol{f}_{\max}}(\phi_{\max} + 2\boldsymbol{n}\pi) \tag{7}$$

for the maximum point. Finally, the sound velocity at each frequency is calculated as

$$c = \left(\frac{1}{c_0} - \frac{\phi_{\min}}{4\pi f_{\min} d} \right) \tag{8}$$

$$c = \left(\frac{1}{c_0} - \frac{\phi_{\max}}{4\pi f_{\max} d} \right) \tag{9}$$

The specimen was first scanned by the conventional SAM, and the obtained image was compared with an optical microscope image of the neighboring section. The same specimen was then scanned with sound speed acoustic microscopy in order to visualize the same area. These two types of images were broadly compared and the frequency-dependent characteristics of the amplitude and phase of a region of interest were also compared.

3. Results

Figure 6 shows (a) optical microscopic image, (b) attenuation image from conventional SAM, (c) sound speed image from conventional SAM, (d) intensity image from sound speed SAM, and (e) sound speed image from sound speed SAM of a rat cardiac allograft model. Figure 6(a) shows that the left part (inner part) is necrotic tissue with hyaline degeneration, and the right part (outer part) is normal myocardium. In Fig. 6(b), the attenuation was 0.8 dB/mm/MHz in the necrotic tissue and 1.2 dB/mm/MHz in the normal myocardium. In Fig. 6(c), the sound speed was 1580 m/s in the necrotic tissue and 1610 m/s in the normal myocardium. An intensity image was generated by two-dimensional distribution of a peak signal amplitude. As a result, the information of the image was different from that of the attenuation image obtained using conventional SAM. In Fig. 6(e), the sound speed was 1580 m/s in the necrotic tissue and 1610 m/s in the normal myocardium.

4. Discussion

In the present study, the entire image of a particular portion obtained using a conventional acoustic microscope was compared with a corresponding image of the same portion obtained using a sound speed microscope. The frequency dependency of amplitude and phase at the same ROI in a specimen was also compared by the frequency variation and Fourier transform methods.

The sound speed image obtained by sound speed microscopy corresponded well to that obtained by conventional SAM. Lesions with hyaline degeneration showed lower sound speed when compared with that of normal myocardium. Frequency domain analysis of amplitude and phase by both methods also showed similar characteristics. The data acquisition time of a frame was 8 s in conventional SAM and 121 s in sound speed microscopy. However, more than ten hours were required to calculate the quantitative values of attenuation and sound speed of an image by conventional SAM, while the same calculation was performed in less than a minute by sound speed microscopy. Conventional SAM requires a skilled operator, for example, to correct the tilting of specimens. The tilt is automatically corrected in sound speed microscopy, and the interface is user-friendly and can be easily operated by medical and pathological researchers.

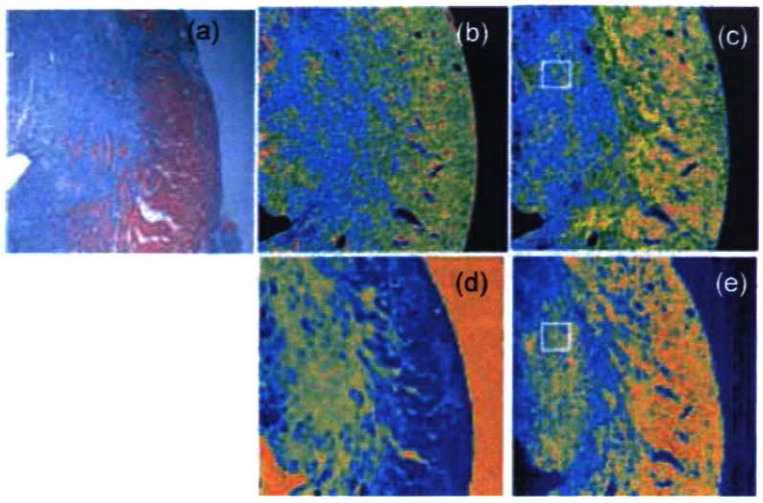

Fig. 6. (a) Optical microscopic image, (b) attenuation image of conventional SAM, (c) sound speed image of conventional SAM, (d) intensity image of sound speed SAM, and (e) sound speed image of sound speed SAM, of a rat cardiac allograft model. ROIs are shown in Fig. 6(c) and (e).

5. Conclusions

An acoustic microscope system that can measure the sound speed of thin slices of biological material was developed. It was a unique acoustic microscope because it used a single pulse and the Fourier transform to calculate the sound speed at all measuring points. Although the data acquisition time of a frame was greater than that in conventional SAM, the total time required for calculation was significantly shorter. The acoustic microscope system can be applied to intraoperative pathological examination.

References

[1] Y. Saijo, M. Tanaka, H. Okawai and F. Dunn, The ultrasonic properties of gastric cancer tissues obtained with a scanning acoustic microscope system, *Ultrasound Med Biol* **17** (1991), 709–714.
[2] H. Sasaki, M. Tanaka, Y. Saijo, H. Okawai, Y. Terasawa, S. Nitta and K. Suzuki, Ultrasonic tissue characterization of renal cell carcinoma tissue, *Nephron* **74** (1996), 125–130.
[3] Y. Saijo, M. Tanaka, H. Okawai, H. Sasaki, S. Nitta and F. Dunn, Ultrasonic tissue characterization of infarcted myocardium by scanning acoustic microscopy, *Ultrasound Med Biol* **23** (1997), 77–85.
[4] Y. Saijo, H. Sasaki, H. Okawai, S. Nitta and M. Tanaka, Acoustic properties of atherosclerosis of human aorta obtained with high-frequency ultrasound, *Ultrasound Med Biol* **24** (1998), 1061–1064.
[5] Y. Saijo, H. Sasaki, M. Sato, S. Nitta and M. Tanaka, Visualization of human umbilical vein endothelial cells by acoustic microscopy, *Ultrasonics* **38** (2000), 396–399.
[6] Y. Saijo, T. Ohashi, H. Sasaki, M. Sato, C.S. Jorgensen and S. Nitta, Application of scanning acoustic microscopy for assessing stress distribution in atherosclerotic plaque, *Ann Biomed Eng* **29** (2001), 1048–1053.
[7] H. Sasaki, Y. Saijo, M. Tanaka and S. Nitta, Influence of tissue preparation on the acoustic properties of tissue sections at high frequencies, *Ultrasound Med Biol* **29** (2003), 1367–1372.
[8] Y. Saijo, T. Miyakawa, H. Sasaki, M. Tanaka and S. Nitta, Acoustic properties of aortic aneurysm obtained with scanning acoustic microscopy, *Ultrasonics* **42** (2004), 695–698.
[9] H. Sano, Y. Saijo and S. Kokubun, Material properties of the supraspinatus tendon at its insertion – A measurement with the scanning acoustic microscopy, *J Musculoskeletal Res* **8** (2004), 29–34.
[10] N. Hozumi, R. Yamashita, C.K. Lee, M. Nagao, K. Kobayashi, Y. Saijo, M. Tanaka, N. Tanaka and S. Ohtsuki, Time-frequency analysis for pulse driven ultrasonic microscopy for biological tissue characterization, *Ultrasonics* **42** (2004), 717–722.

Technology and Health Care 13 (2005) 331–344
IOS Press

Detection and correction of aliasing in ultrasonic measurement of blood flows with Ultrasonic-Measurement-Integrated simulation

Kenichi Funamoto[a], Toshiyuki Hayase[b,*], Yoshifumi Saijo[c] and Tomoyuki Yambe[c]
[a]*Graduate School of Engineering, Tohoku University, Sendai, Japan*
[b]*Institute of Fluid Science, Tohoku University, Sendai, Japan*
[c]*Institute of Development, Aging and Cancer, Tohoku University, Sendai, Japan*

Abstract. Detailed information of real blood flows is essential to develop an accurate diagnosis or treatment for serious circulatory diseases such as aortic aneurysms. *Ultrasonic-Measurement-Integrated (UMI) simulation*, in which feedback signals from the ultrasonic measurement make the simulation converge to the real blood flow, is a key to solving this problem. However, aliasing in the ultrasonic blood velocity measurement causes UMI simulation to converge to an erroneous result. In this paper, we have investigated the detection and the correction of aliasing in UMI simulation. The artificial force in the feedback of UMI simulation can be used as an index to detect the aliasing. We have proposed two ways for the correction of the aliasing. Correction A, in which measurement velocity is replaced with the computational one at the monitoring point where the aliasing is detected, substantially improves the accuracy of UMI simulation. Correction B, in which measurement velocity is replaced with an estimated Doppler velocity, can provide exactly the same result as that of UMI simulation using the nonaliased standard solution. Although correction B gives the most accurate result, correction A seems more robust and, therefore, a beneficial choice considering the other artifacts in the measurement.

1. Introduction

Recently, many researches have focused on the relationship between circulatory diseases and hemodynamics, such as the development, progress, and rupture of aneurysm and wall shear stress [1–4]. For elucidation, the numerical simulation of blood flow has been performed extensively using realistic vessel geometries obtained by medical imaging techniques such as magnetic resonance imaging (MRI) or computed tomography (CT) [5–9]. These studies have provided many insights into the relationship. However, it is difficult for ordinary numerical simulations to exactly reproduce the real blood flow because of an inherent problem of specification of the boundary conditions as well as problem in modeling of complex blood flow problems [6].

For the measurement of blood flows, ultrasonic diagnostic equipment is the most widely used for the diagnosis of blood vessel diseases among all imaging technologies. It can non-invasively provide real-time images of the blood flow and vessel configuration *in vivo* by color Doppler ultrasonography [10].

*Address for correspondence: Dr. T. Hayase, Institute of Fluid Science, Tohoku University, 2-1-1 Katahira, Aoba-ku, Sendai, Miyagi 980-8577, Japan. Tel./Fax: +81 22 217 5253; E-mail: hayase@ifs.tohoku.ac.jp.

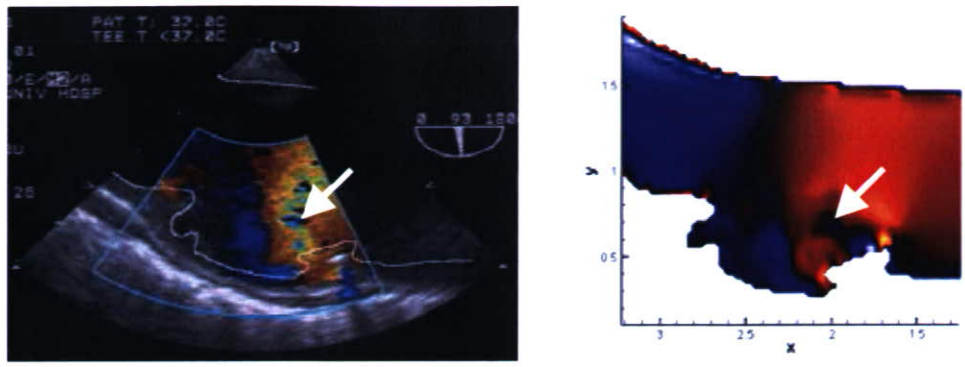

(a) (b)

Fig. 1. (a) Color Doppler image around a thoracic aneurysm (Center frequency f_C: 4.4 MHz, Pulse repetition frequency f_R: 4 kHz) and (b) that of UMI simulation.

However, the blood flow measurement is limited to the velocity component in the ultrasonic beam direction or Doppler velocity, since it converts the Doppler shift frequency to the velocity. The blood flow is visualized by color Doppler image which displays colors of graduated intensity, blue for flow away from the probe and red for flow approaching the probe for instance, superimposing on the B-mode image, which shows the configuration of the blood vessel wall with gray scale, as shown in Fig. 1(a). Unfortunately, it is difficult to recognize the exact three-dimensional structure of the blood flow from the color Doppler image.

In order to solve those problems both in numerical simulation and in measurement as described above, Ultrasonic-Measurement-Integrated (UMI) simulation has been proposed by the present authors [11]. It integrates the color Doppler ultrasonography and numerical simulation and makes it possible to reproduce the blood flow on a computer. During the computational process, feedback signals are generated from the difference between the output signals of the measurement and those of the computation, and are added to the simulation to compensate for the difference. In the former study [11], the characteristics of UMI simulation are studied in a two-dimensional model problem, showing that the result of UMI simulation in feedback domain rapidly converges to the standard solution, even with usually incorrect upstream boundary condition. We also carried out UMI simulation with feedback from real color Doppler measurement and showed good agreement with measurement. In that study, it is observed that UMI simulation follows the measurement data even if it includes the aliasing as shown with white arrow in Fig. 1(b). In fact, the reproduction of aliasing is not desirable since the aliasing region originally shows incorrect data.

In the color Doppler ultrasonography, aliasing occurs in the region where Doppler velocity exceeds the limitation of the measurable velocity. As a result, aliasing region is displayed with incorrect color in the color Doppler image. The elimination of the aliasing is a serious issue for accurate quantification of regurgitation of heart valves in the cardiovascular diagnosis and many methods have been proposed for this problem [12–14]. Fan et al. [13] proposed a new technology termed Quantitative Un-Aliased Speed Algorithm Recognition (Quasar), which employs two color Doppler imaging with two different ultrasound frequencies simultaneously and compute a new operating frequency based on the difference between the two phase shifts for each frequency. Though it allows the measurement of high blood flow velocities accurately during transesophageal color Doppler ultrasonography, it cannot follow the disturbed flow. Stewart [14] performed iterative curve fitting of the jet including the aliasing to a

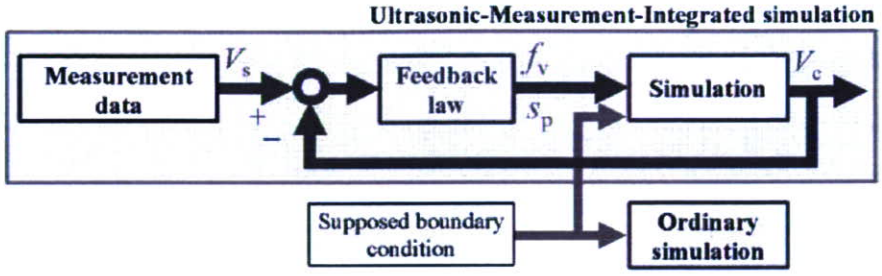

Fig. 2. Block diagram of Ultrasonic-Measurement-Integrated simulation.

mathematical model derived from the jet theory, and distinguished the nonaliased velocities from the aliased ones in steady trial. However, it is difficult to construct the mathematical model when the geometry is complicated or the flow is disturbed.

In this paper, the detection and the correction of the aliasing in UMI simulation are proposed. Magnitude of the feedback in UMI simulation is used as index in determining the aliasing. Two methods are proposed for correction of aliasing. Validation of the proposed methods is examined with a simple two-dimensional model problem for blood flow in an aorta with an aneurysm. A standard solution is first defined as a model of real flow. Aliasing is introduced to the standard solution. The UMI simulation is carried out with the aliased standard solution applying two correction methods after detection of aliasing. For the verification of the effectiveness by the presented algorithms in UMI simulation, UMI simulation without correction, the ordinary simulation and UMI simulation with nonaliased standard solution are also performed.

2. Method to correct aliasing in UMI simulation

2.1. UMI simulation

Ultrasonic-Measurement-Integrated (UMI) simulation is a kind of flow observer to reproduce the real blood flow numerically [15]. The UMI simulation consists of numerical simulation and measurement of blood flow with color Doppler ultrasonography as shown in Fig. 2. During the computational process, the difference between color Doppler images obtained by measurement and simulation is fed back to the numerical simulation. The UMI simulation allows not only reconstruction of the color Doppler image but also the determination of the velocity vectors and the pressure distribution in detail. The following is a brief explanation of this methodology in 2-dimensional formulation. Detailed description is given in another article [11].

As described above, measurement data is obtained by the color Doppler ultrasonography. It can provide real-time images of the anatomy and the blood flow structure simultaneously. The configuration of the blood vessel wall *in vivo* is reconstructed as a B-mode image from time delays and magnitudes of the ultrasonic echo. In addition to that, the blood velocity component in the ultrasonic beam direction, namely the Doppler velocity, is measured by the Doppler shift frequency. For the visualization of the blood flow, the frequency shifts are converted to colors of graduated intensity as shown in Fig. 1(a).

In the numerical simulation, the governing equations are the Navier-Stokes equations for incompressible and viscous fluid flow,

$$\frac{\partial \mathbf{u}}{\partial t} = -(\mathbf{u} \cdot \text{grad})\mathbf{u} + \frac{1}{Re}\nabla^2 \mathbf{u} - \text{grad}p, \tag{1}$$

and the equation of continuity,

$$\mathrm{div}\mathbf{u} = 0, \tag{2}$$

where $\mathbf{u} = (u, v)$ is the velocity vector and p is the pressure. They are discretized by means of the finite volume method and are solved with an algorithm similar to the SIMPLER method [16]. In SIMPLER method, x-directional momentum equation is expressed as

$$u_i = (\Sigma B_j u_j + S_i)/B_i + d_i(p_i - p_{i-1}), \tag{3}$$

where $(\Sigma B_j u_j)$ means the summation of the four values circumfusing u_i. By substituting Eq. (3) and similar equations for y-directional momentum to the integrated form of the equation of continuity, the pressure equation is obtained as

$$a_i p_i = \Sigma a_j p_j + s_{pi}, \tag{4}$$

where $(\Sigma a_j p_j)$ means the summation of the values at four adjacent nodes. The notations of the parameters in Eqs (3) and (4), as well as supplementary pressure correction equations and velocity correction procedure in SIMPLER method are explained in a reference [17].

In order to compensate for the difference between the computation and the measurement, feedback signals are applied to the governing equations in the form of source terms. The feedback algorithm consists of feedback to the velocity and pressure fields as follows. As a feedback signal, the artificial force f_v proportional to the difference between Doppler velocities of the measurement and the simulation is applied to the Navier-Stokes equations in the direction of the ultrasonic beam. The force f_v is calculated by the following equation:

$$f_v = -K_v \rho (V_c - V_s) u'_{\max} \Delta S, \tag{5}$$

where K_v is the feedback gain (nondimensional), $u'_{\max}$ is the maximum average flow velocity of the blood flow at the upstream boundary, and ΔS is an interfacial area of the control volume. Here, the artificial force f_v accelerates the fluid to reduce the error in velocity and increases the pressure of the control volume through the pressure Eq. (4). Hence, the other additional feedback signal s_p is introduced to the pressure equation as the source term to counteract the effect of artificial force f_v.

$$s_p = -K_p \rho (V_c - V_s) \Delta S, \tag{6}$$

where K_p is the feedback gain for the pressure (nondimensional).

The calculation of the feedback signal is illustrated in Fig. 3. The purpose of the feedback is to force the velocity $\mathbf{u}_c$ obtained by numerical simulation to converge to the real flow velocity $\mathbf{u}_s$ obtained with ultrasonic diagnostic equipment. The Doppler velocities of the numerical simulation and the measurement, V_c and V_s, are the projection of $\mathbf{u}_c$ and $\mathbf{u}_s$ in the ultrasonic beam direction (a chain line in Fig. 3), respectively. If the computational result V_c is smaller than V_s, the artificial force f_v has a positive value and accelerates the fluid in the ultrasonic beam direction in UMI simulation to reduce the error. The force f_v is decomposed to the x-directional component f_{vx} and the y-directional component f_{vy}, which are added to the control volumes of $u(i, j)$ and $v(i, j)$ in the Navier-Stokes equation, respectively.

For the evaluation of UMI simulation, we define the average error norms $\bar{e}_N$ for an arbitrary variable a, which is the velocity component u, v, V, the velocity vector $\mathbf{u}$ or the pressure p as follows:

$$\bar{e}_N(a) = \frac{1}{N} \sum_n \frac{1}{a_{\max} T} \int_T |a_{cn}(t) - a_{sn}(t)| dt, \tag{7}$$

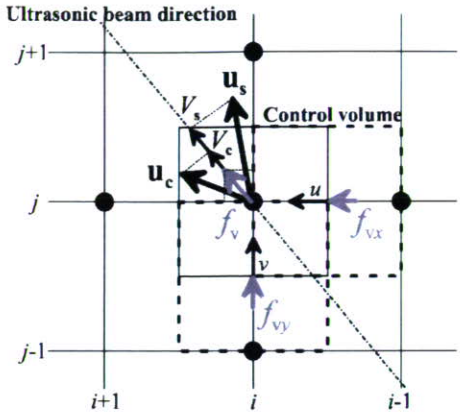

Fig. 3. Computational grid and definition of calculation of feedback signal.

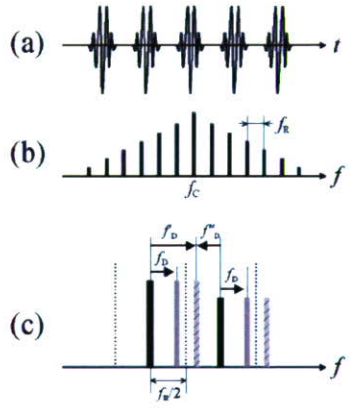

Fig. 4. Schematic diagram of (a) repeated pulse of ultrasound, (b) power spectrum, and (c) Doppler shift.

where N is the total number of the monitoring points, T is the characteristic time, $|\cdot|$ is the absolute value for scalar variables or l_1 norm $|u| + |v|$ for the velocity vector $\mathbf{u}$, $a_{\max}$ is the characteristic value for normalization: $a_{\max} = u'_{\max}$ for velocity or $a_{\max} = \rho u'^2_{\max}$ for pressure. Subscript cn corresponds to UMI simulation, and sn to the measurement, respectively. In the subscripts "cn" and "sn", n is the index of the grid point.

The UMI simulation is specified by the combination of gains (K_v, K_p). Note that the special case with $K_v = K_p = 0$ corresponds to the ordinary simulation without feedback. The values of the gains (K_v, K_p) are determined so that the average error norms $\bar{e}_N(a)$ of some specified variables takes the minimum value over a number of trial computations. The improvement of the computational accuracy by UMI simulation is also evaluated using $\bar{e}_N(a)$ of some specific variables.

2.2. *Correction of aliasing*

Aliasing is a serious error in Doppler measurement resulting in an incorrect magnitude and direction of the velocity. Figure 4 explains the cause of the aliasing. Repeated pulses of ultrasound are emitted from the probe as shown in Fig. 4(a). This ultrasound has a power spectrum with center frequency f_C and pulse repetition frequency interval f_R as shown in Fig. 4(b). In the Doppler velocity measurement,

the Doppler velocity is calculated from the Doppler shift frequency f_D as shown in Fig. 4(c). In case that the Doppler shift frequency f'_D exceeds one half the pulse repetition frequency ($f_R/2$), it is regarded as the Doppler shift from the adjacent frequency (f''_D) and therefore, it leads to the Doppler velocity with incorrect magnitude and direction. Therefore, the measurable Doppler velocity V is expressed as

$$V_{\min} \leqslant V \leqslant V_{\max}, \tag{8}$$

where $V_{\max}$ and $V_{\min}$ are the positive and negative threshold values of measurable Doppler velocity, respectively, and those are determined according to the pulse repetition frequency f_R as shown in Eq. (9).

$$\begin{cases} V_{\max} = \dfrac{cf_R}{4f_C \cos\theta} \\ V_{\min} = -\dfrac{cf_R}{4f_C \cos\theta} \end{cases}, \tag{9}$$

where c is the acoustic velocity and θ is an irradiation angle of ultrasound to the blood flow. In the case that V is larger than $V_{\max}$, the Doppler velocity is regarded as $V_{\min} + (V - V_{\max})$ with the opposite direction. In the case that V is smaller than $V_{\min}$, a similar occurs.

In the former study [11], it was observed that the intensity of the feedback signal $|f_v|$ becomes very large in the region where the aliasing occurs. Here, we use the feedback signal f_v for the detection and the correction of the aliasing. In case that the artificial force f_v calculated by Eq. (5) at a monitoring point is in a normal range,

$$f_{\min} \leqslant f_v \leqslant f_{\max}, \tag{10}$$

where $f_{\min} = K_v \rho V_{\min} u'_{\max} \Delta S$ and $f_{\max} = K_v \rho V_{\max} u'_{\max} \Delta S$, f_v is used for the feedback in UMI simulation with no corrections. In contrast, if f_v is outside the normal range, $f_v < f_{\min}$ or $f_{\max} < f_v$, it is regarded as an unnatural force in the opposite direction due to the aliasing of measured Doppler velocity. In this case, we introduce two ways of correcting the measured Doppler velocity V_s in the feedback in Eqs (5) and (6) as follows.

Correction A: *The measured Doppler velocity is replaced with calculated value as*

$$V_s = V_c. \tag{11}$$

Correction B: *The measured Doppler velocity is replaced with the estimated Doppler velocity considering the effect of the aliasing as*

$$V_s = V_e, \tag{12}$$

where

$$V_e = \begin{cases} V_{\max} - (V_{\min} - V_s) \ (f_v < f_{\min} < 0 \\ V_{\min} - (V_{\max} - V_s) \ (0 < f_{\max} < f_v) \end{cases}. \tag{13}$$

For example, in case that the f_v is smaller than the negative threshold value $f_{\min}$, the Doppler velocity V_s is thought to take the incorrect negative value because of aliasing. We convert the velocity to the positive value by Eq. (13), and apply the feedback signal there using the recalculated positive artificial force f_v.

Table 1
Computational conditions

Heart rate	0.87 Hz (52 beat/min)
Cardiac cycle T	1.15 s
Cardiac output	9.17×10^{-5} m^3/s (5.5 l/min)
Entrance flow	6.42×10^{-5} m^3/s (3.85 l/min)
Average velocity at maximum flow rate u'_{max}	0.74 m/s
Entrance vessel diameter D	28.25×10^{-3} m
Kinematic viscosity ν	4.0×10^{-6} m^2/s

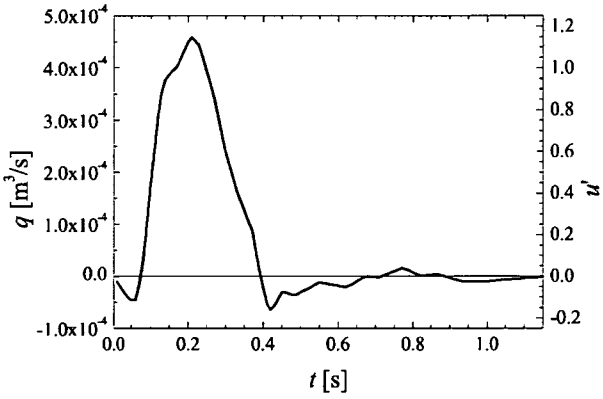

Fig. 5. Time variation of flow volume in descending aorta and of cross-sectional average flow velocity at upstream boundary.

3. Numerical simulation of correction of aliasing

3.1. Formulation

In this section, we investigate the effectiveness of the proposed method to detect and correct the aliasing signal using the feedback intensity in UMI simulation. For that purpose, we carry out UMI simulation using a simple two-dimensional model problem for blood flow in the descending aorta with an aneurysm. The shape of blood vessel is obtained by transesophageal ultrasonography with an ultrasound device (SONOS 5500, Philips Medical Systems, Andover, MA, USA) with transesophageal ultrasonic transducer (T6210, Philips Medical Systems, Andover, MA, USA). Table 1 summarizes parameters used in this computation. Among them, heart rate and cardiac output are measured during the ultrasonic measurement. Cardiac cycle T is calculated from the heart rate. The upstream shape of the blood vessel is assumed to be cylindrical in order to determine two-dimensional inlet velocity profile according to the three-dimensional time varying flow rate data, and the diameter D is calculated from the image. We assume that 30% of the cardiac output flows into the branches and that the remaining 70% (6.42×10^{-5} m^{3}s^{-1}) flows into the descending aorta referring to the blood flow measurement data [18]. The variation of the flow rate q is modeled as shown in Fig. 5 according to the MR measurement by Olufsen et al. [19]. Blood is assumed to be a Newtonian fluid with density $\rho = 1.00 \times 10^3$ kgm^{-3} and dynamic viscosity $\mu = 4.0 \times 10^{-3}$ Pas.

All the values are nondimensionalized with the diameter of the blood vessel D, the cross-sectional average velocity u_{max} at the upstream boundary for the maximum cardiac output, and the kinematic vis-

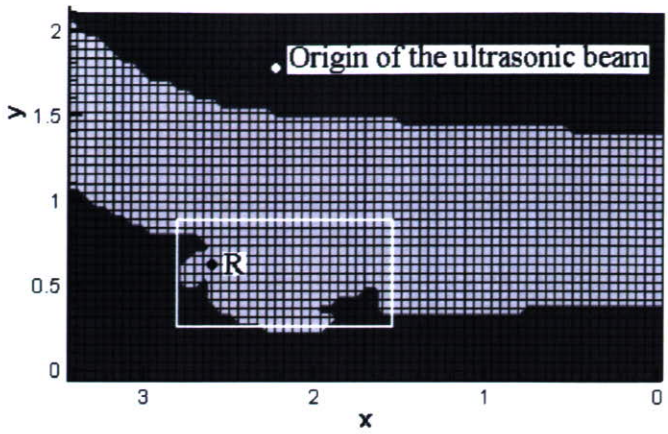

Fig. 6. Computational grid and monitoring region in which monitoring points for feedback are arranged.

cosity ν of the blood. From here on, the same symbols are used for both dimensional and nondimensional values without confusion.

In order to define a two-dimensional computational domain, the B-mode image of the blood vessel obtained by ultrasonic diagnostic equipment is digitized to extract the cross-sectional surface manually, and the pixel data is allocated in a staggered grid system with uniform grid spacing as shown in Fig. 6. In this research, we introduce a grid of 65 $\times$ 40 points in x and y directions with grid spacing of 1.487 $\times$ 10^{-3} m in each direction, compromising between the reproducibility of the vessel shape and the computational time. The origin of the ultrasonic beam, where ultrasound is emitted from the probe, is set at the same position as the measurement [see the center of a sector in Fig. 1(a)].

First, we perform a numerical simulation to obtain a standard solution, or a model of real blood flow. The velocity profile at the upstream boundary in calculating the standard solution was determined from a three-dimensional steady blood flow simulation in the extended blood vessel consisting of ascending aorta, aortic arch, descending aorta and abdominal aorta with commercial computational fluid dynamics software (FLUENT 6.1.22, Fluent Inc., Lebanon, NH, USA). In the steady numerical simulation with FLUENT, inflow velocity is set at 20 cms^{-1}, which is the mean value of blood velocity in the aorta. At the downstream boundary of the standard solution, a free-flow condition ($\partial/\partial n = 0$, n: coordinate normal to the boundary) is applied, and a no-slip condition is applied to the blood vessel wall. The adequate residual at convergence and the maximum iteration number are respectively determined as 1 $\times$ 10^{-5} and 300 after test computations. It is noted that the condition to obtain the standard solution is the same as that of the former paper [11] except that Poiseuille flow is assumed at the entrance in the previous study. In this paper, we apply the other velocity profile as shown in Fig. 7 at each time step in order to calculate under more realistic condition. After the computation of the standard solution, aliasing is artificially introduced in the standard solution, setting the threshold values, $V_{\max}$ and $V_{\min}$, and processing all Doppler velocity data not to excess the threshold vales in manner of wraparound the Doppler velocity scale.

For UMI simulation, the uniform velocity profile is applied at the upstream boundary. The other computational conditions are the same as that of the standard solution. In the UMI simulation, discrepancy caused by the incorrect upstream boundary condition is compensated for by the feedback action and the result approaches that of the standard solution in the region of feedback. In this study, we define the rectangular arrangement of monitoring points for the feedback covering the aneurysm which consists of all 325 points in the white rectangular region as shown in Fig. 6 to reproduce the blood flow in the region.

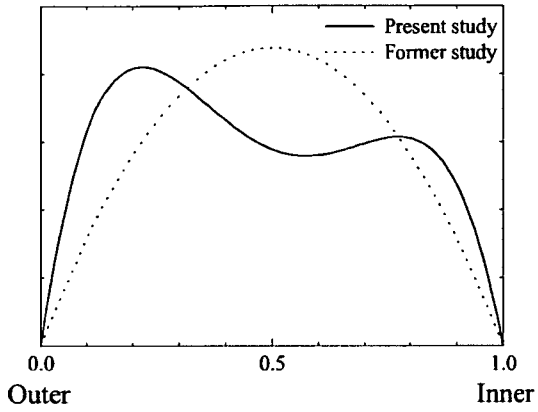

Fig. 7. The x-directional velocity profile at the upstream boundary.

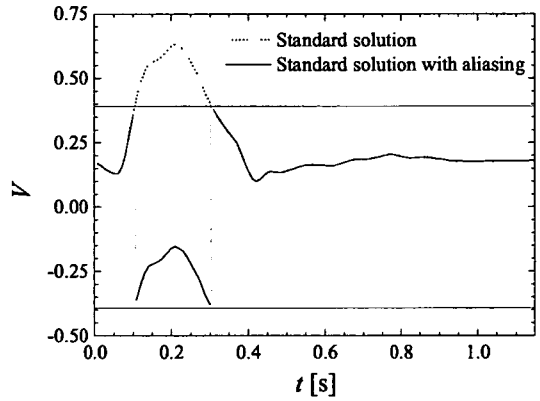

Fig. 8. Variation of Doppler velocity of nonaliased or aliased standard solution at monitoring point R.

The representative monitoring point R, where the aliasing is observed in the aliased standard solution, is also chosen in the monitoring region to observe the variation of any variables.

3.2. Results and discussion

The numerical simulation to obtain the standard solution takes more than 26 cardiac cycles to converge to the periodic oscillation. We define the standard solution as the repetition of the result in the 26th cardiac cycle. Figure 8 shows Doppler velocity of the standard solution at point R (see Fig. 6).

First, we investigated the detection of the aliasing. Based on the method described in previous section, we artificially introduce aliasing for this standard solution. In this study, the threshold values of Doppler velocity, $V_{\max}$ and $V_{\min}$, are set $\pm$ 25 cms^{-1} (0.392 in the nondimensional value). In Fig. 8, horizontal lines mean the nondimensional threshold values.

Figure 9(a) shows three snapshots of the color Doppler image in the monitoring region (white rectangular region in Fig. 6) in one cardiac cycle for the standard solution in which aliasing is introduced. In the preceding two images, the aliasing can be observed. The regions where the aliasing is introduced are shown with volume rendering in Fig. 9(b). The blue regions mean the exceeding the upper threshold value, the red region means below the lower threshold value, and the green lines mean the vessel wall.

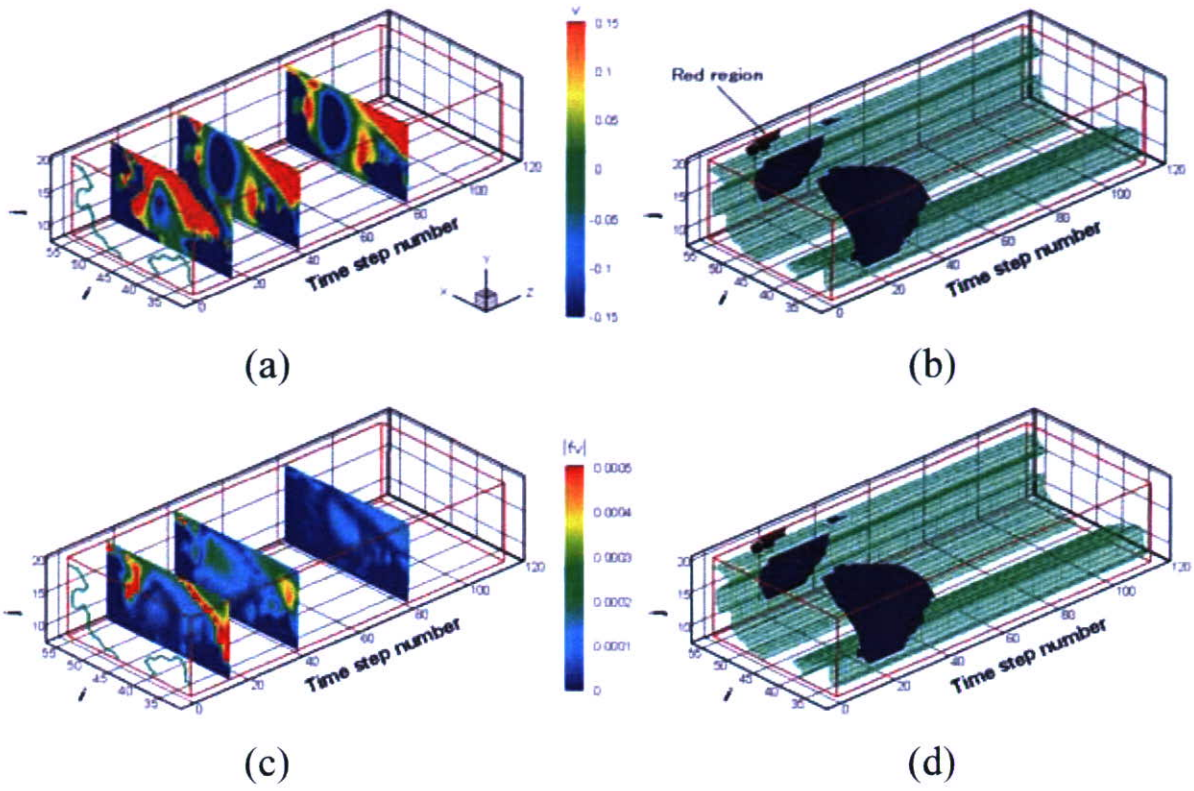

Fig. 9. Distribution of variables in the monitoring region in one cardiac cycle: (a) color Doppler images at $t = 0.15$ s in acceleration phase, and $t = 0.40$ s and 0.80 s in deceleration phase, (b) volume rendering of aliasing region, (c) feedback intensity in the first cardiac cycle of UMI simulation using aliased standard solution at the same timing as that of (a), and (d) volume rendering of the region where aliasing is detected by UMI simulation with correction B.

In the vicinity of the time step number 21 ($t = 0.21$ s) at which maximum flow rate occurs, the aliasing regions spread in the upstream and downstream area of the monitoring region.

The UMI simulation is performed using the aliased standard solution. The optimum combination of gains (K_v, K_p) is determined as (0.4, 0.4) to minimize the average error norms $\bar{e}_N(\mathbf{u})$ of the velocity vector based on the result of the former research [11]. All UMI simulations described below are carried out with these values of gains. The instantaneous feedback intensity $|f_v|$, which is the average absolute value of the artificial force f_v during a time step in the first cardiac cycle as shown in Fig. 9(c) becomes relatively high in the region where aliasing occurs in Fig. 9(a). By using this unnatural feedback signal as the index of the aliasing, we performed UMI simulation with correction. The area where the aliasing is detected by UMI simulation with correction B is shown in Fig. 9(d). Figure 9(d) completely agrees with Fig. 9(b), implying that all aliasing introduced regions are detected correctly.

Correction of aliasing in UMI simulation is evaluated as follows. Color Doppler image of the nonaliased and aliased standard solution at peak flow ($t = 0.21$ s) are shown in Fig. 10. Here, note that the maximum and minimum values of the color bar do not correspond to $V_{\max}$ and $V_{\min}$, respectively, to emphasize the difference in the color Doppler images clearly. Corresponding color Doppler images of UMI simulations are shown in Fig. 11. Figure 11(a) shows the color Doppler image obtained without feedback of UMI simulation (ordinary simulation), and Fig. 11(b) and (c) show those of UMI simulations without correction of aliasing and with correction B, respectively. Since the applied upstream boundary

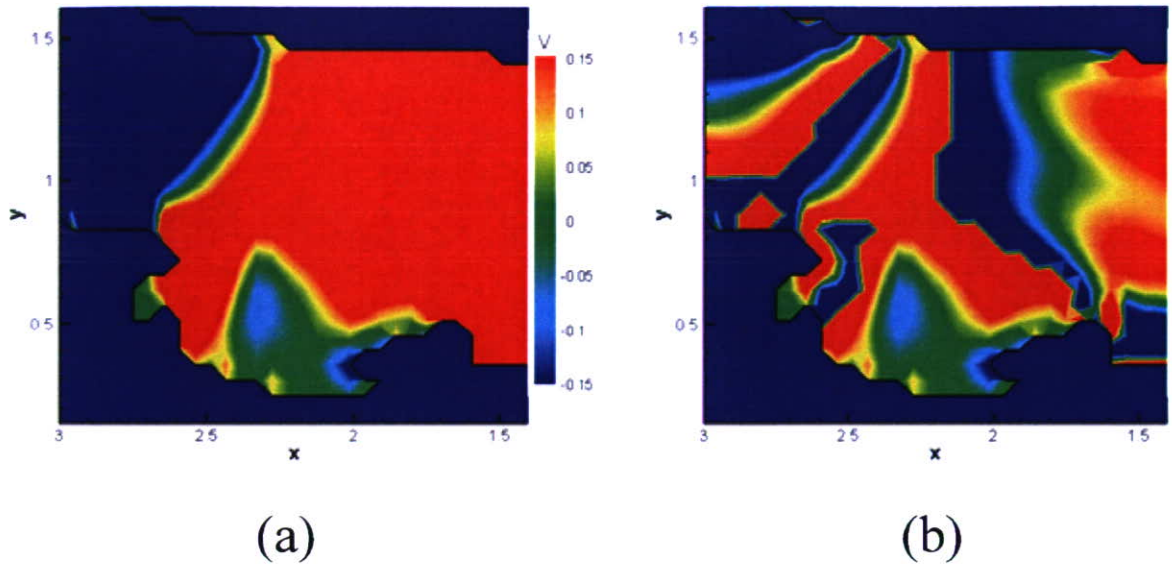

Fig. 10. Comparison of (a) color Doppler image around an aneurysm at peak flow of standard solution without aliasing and (b) that with aliasing.

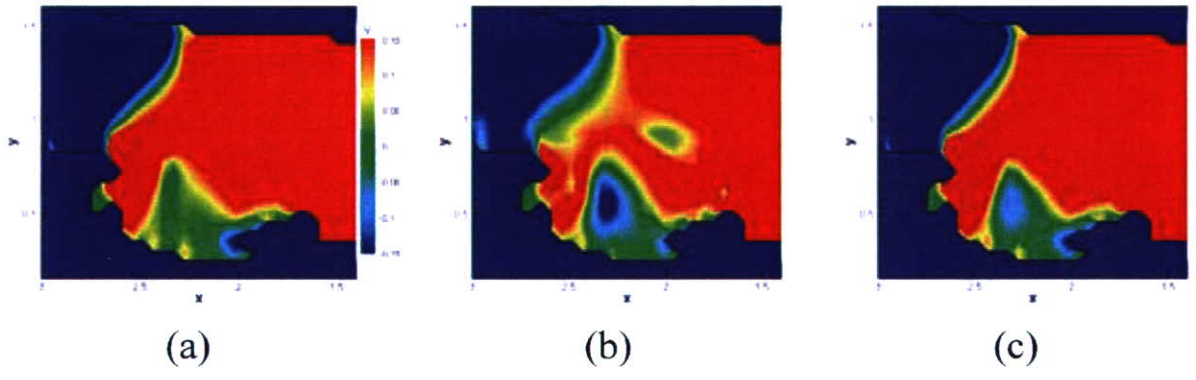

Fig. 11. Comparison of (a) color Doppler image around an aneurysm at peak flow of UMI simulation without feedback (ordinary simulation), and (b) and (c) those of UMI simulations without correction of aliasing and with correction B, respectively.

condition is not so different between the standard solution and UMI simulations, Figs 10(a) and 11(a) are similar to each other, but the different color pattern is visible in the aneurysm. The color Doppler image of UMI simulation without correction at peak flow [Fig. 11(b)] shows an erroneous result. In contrast, UMI simulation with correction B [Fig. 11(c)] correctly reproduces the standard solution [Fig. 10(a)]. The result of UMI simulation with correction A is similar to that of correction B showing good agreement with the standard solution, although it is omitted here because of page limitation.

Variation of the velocity components and the pressure at point R in one cardiac cycle is shown in Fig. 12. The velocity components of the ordinary simulation with dotted line are different from those of the standard solution with bold line. UMI simulations with correction A and B, which almost overlap each other, closely converges to the standard solution, while the UMI simulation without correction shows the result completely different from those of the standard solution and even worse than the

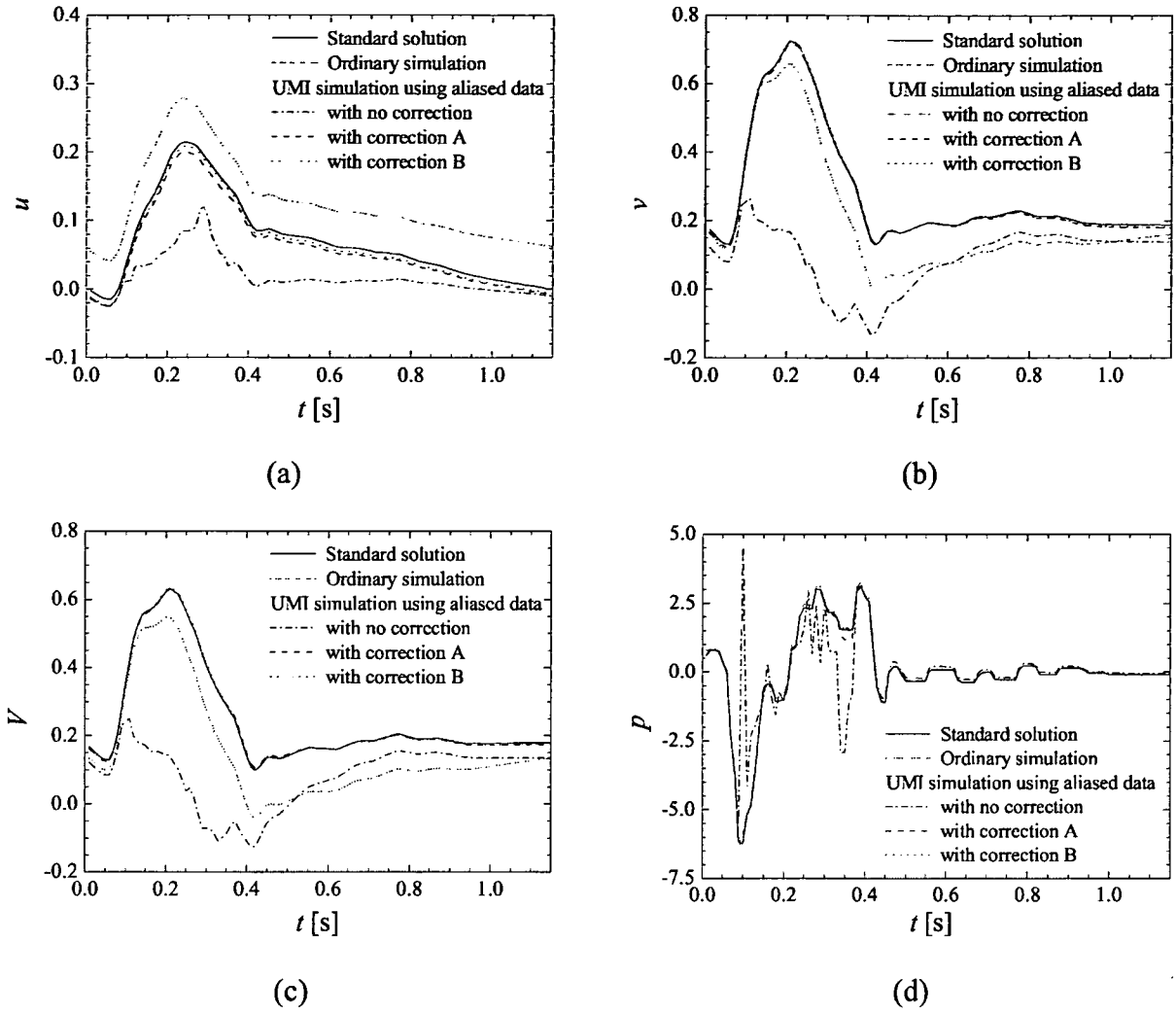

Fig. 12. Comparison of periodic solutions of (a) x-directional velocity u, (b) y-directional velocity v, (c) Doppler velocity V, and (d) pressure p at monitoring point R. The UMI simulations used the aliased standard solution.

ordinary simulation. At the point R where the results are observed, the aliasing occurs from $t = 0.11$ s to 0.30 s. However, the timing when the error against the standard solution enlarges is earlier than $t = 0.11$ s. This is because the result at the point R is affected by the aliasing data which is fed back to UMI simulation at the other monitoring points. The influence of the aliasing on the result is also observed at the other monitoring points where aliasing does not occur through one cardiac cycle, skewing the velocity components from those of the standard solution and perturbing the pressure.

For the quantitative comparison between these results, the average error norms calculated by Eq. (7) are summarized in Table 2. The UMI simulation using aliasing data with no correction does not improve the computational accuracy comparing to those of the ordinary simulation. On the other hand, the results of UMI simulations with corrections A and B improve the computational accuracy about the velocity vectors. Correction A is simple to apply and provides results similar to that of correction B. It is noted that UMI simulation with correction B gives the result exactly the same as that of the UMI simulation with

Table 2
Comparison of average error norm

	u	v	V	p
Standard solution	0	0	0	0
Ordinary simulation	1	1	1	1
UMI simulation using aliased data				
– with no correction	2.758	1.625	1.373	29.086
– with correction A	0.447	0.212	0.180	1.787
– with correction B	0.369	0.162	0.136	1.031
UMI simulation using nonaliased data	0.369	0.162	0.136	1.031

the nonaliased standard solution, which is the best result in UMI simulation in terms of the reproduction of the standard solution. The errors in the velocity components are reduced by the application of UMI simulation to 37% for u, 16% for v, and 14% for V of those of the ordinary simulation. Here, the accuracy of the y-directional velocity component v is more improved than the x-directional velocity component u since the origin of the ultrasonic beam is located in the y-direction of the monitoring region, and therefore, Doppler velocity V includes more information of v than u. In contrast, though the error of the pressure becomes large when UMI simulation is carried out, it is not a crucial problem because those values are very small as seen in Fig. 12(d).

In the present model problem, aliasing can be detected from the instantaneous feedback signal f_v in UMI simulation, and aliasing can be corrected with two correction methods. Considering the false recognition of the fully disturbed flow as the aliasing or the effect of the other artifacts, UMI simulation with correction B may lead incorrect results due to its correction process. On the other hand, UMI simulation with correction A only prevents all suspect data from being introduced into UMI simulation, and there is no possibility that the application of feedback contrary lead UMI simulation to the incorrect results. Hence, correction A can be thought to give a more robust method useful for practical applications.

4. Conclusions

In this paper we investigated the detection and the correction of aliasing of ultrasonic blood velocity measurement in Ultrasonic-Measurement-Integrated (UMI) simulation. A UMI simulation was performed for a two-dimensional model problem using a standard numerical solution with and without artificially introduced aliasing. Aliasing causes UMI simulation to differ from the standard solution and the error may be greater than that of ordinary simulations. The artificial force in the feedback of UMI simulation can be used as an excellent index to detect the aliasing. We proposed two ways for the correction of the aliasing: correction A, in which measurement velocity is replaced with the computational one at the monitoring point where the aliasing is detected, substantially improves the accuracy of UMI simulation; and correction B, in which measurement velocity is replaced with an estimated Doppler velocity at the point, can provide the same result as that of UMI simulation using the nonaliased standard solution. Though correction B yields the most accurate result, correction A seems more robust and, therefore, a beneficial choice considering the other artifacts in the measurement. The present study revealed the potential of UMI simulation to improve the accuracy of the original ultrasonic measurement. For future work, we will extend the proposed method to three-dimensional problems and the application to the real color Doppler ultrasonography in order to develop advanced medical diagnostic and treatment equipment.

Acknowledgements

The present study was supported in part by the Research Fellowships of the Japan Society for the Promotion of Science for Young Scientists #16-3421. The authors would like to thank Assistant Professor N. Asai of the University of Aizu for his assistance in grid generation for the computation with FLUENT. The computations were performed using the supercomputer system SGI ORIGIN 2000 in the Advanced Fluid Information Research Center, Institute of Fluid Science, Tohoku University. The authors are grateful to the staff of the AFI Research Center for their support in the computational work.

References

[1] C.G. Caro, J.M. Fitz-Gerald and R.C. Schroter, Atheroma and arterial wall shear. Observation, correlation and proposal of a shear-dependent mass transfer mechanism for atherogenesis, *Proc. R. Soc. Lond. B Biol. Soci.* **117** (1971), 109–159.
[2] D.N. Ku, D.P. Giddens, C.K. Zarins and S. Glagov, Pulsatile flow and atherosclerosis in the human carotid bifurcation. Positive correlation between plaque location and low oscillating shear stress, *Arteriosclerosis* **5** (1985), 293–302.
[3] D.P. Giddens, C.K. Zarins and S. Glagov, The role of fluid mechanics in the localization and detection of atherosclerosis, *J. Biomech. Eng.* **115** (1993), 588–594.
[4] H.S. Flora, B. Talei-Faz, L. Ansdell, E.J. Chaloner, A. Sweeny, A. Grass and M. Adiseshiah, Aneurysm wall shear stress and tendency to rupture are features of physical wall properties: an experimental study, *J. Endovasc. Ther.* **9** (2002), 665–675.
[5] D.A. Steinman, Image-based computational fluid dynamics modeling in realistic arterial geometries, *Ann. Biomed. Eng.* **30** (2002), 483–497.
[6] Y. Liu, Y. Lai, A. Nagaraj, B. Kane, A. Hamilton, R. Greene, D.D. McPherson and K.B. Chandran, Pulsatile flow simulation in arterial vascular segments with intravascular ultrasound images, *Med. Eng. Phys.* **23** (2001), 583–595.
[7] I. Marshall, S. Zhao, P. Papathanasopoulou, P. Hoskins and X.Y. Xu, MRI and CFD studies of pulsatile flow in healthy and stenosed carotid bifurcation models, *J. Biomech.* **37** (2004), 679–687.
[8] E.S. Di Martino, G. Guadagni, A. Fumero, G. Ballerini, R. Spirito, P. Biglioli and A. Redaelli, Fluid-structure interaction within realistic three-dimensional models of the aneurysmatic aorta as a guidance to assess the risk of rupture of the aneurysm, *Med. Eng. Phys.* **23** (2001), 647–655.
[9] E.A. Finol and C.H. Amon, Blood flow in abdominal aortic aneurysms: pulsatile flow hemodynamics, *J. Biomech. Eng.* **123** (2001), 474–484.
[10] K. Ferrara and G. DeAngelis, Color flow mapping, *Ultrasound Med. Biol.* **23** (1997), 321–345.
[11] K. Funamoto, T. Hayase, A. Shirai, Y. Saijo and T. Yambe, Fundamental study of Ultrasonic-Measurement-Integrated simulation of real blood flow in the aorta, *Ann. Biomed. Eng.* **33** (2005), 413–426.
[12] K.R. Baek, M.H. Bae and S.B. Park, A new aliasing extension method for ultrasonic 2-dimensional pulsed Doppler systems, *Ultrason. Imaging* **11** (1989), 233–244.
[13] P. Fan, N.C. Nanda, R.P. Gatewood, Jr., E.G. Cape and A.P. Yoganathan, Transesophageal color Doppler evaluation of obstructive lesions using the new "Quasar" technology, *Ultrasound Med. Biol.* **21** (1995), 1021–1028.
[14] S.F.C. Stewart, Aliasing-tolerant color Doppler quantification of regurgitant jets, *Ultrasound Med. Biol.* **24** (1998), 881–898.
[15] T. Hayase and S. Hayashi, State estimator of flow as an integrated computational method with the feedback of online experimental measurement, *J. Fluids Eng.* **119** (1997), 814–822.
[16] T. Hayase, J.A.C. Humphrey and R. Greif, *Mini-manual for ROTFLO2*, Dept. Mech. Eng. Rep. FM-90-1, Univ. Calif. Berkeley, 1990.
[17] S.V. Patankar, *Numerical Heat Transfer and Fluid Flow*, Hemisphere Pub. Corp.,Washington DC/New York, 1980.
[18] W.F. Ganong, *Review of Medical Physiology*, (17th ed.), Appleton & Lange, Norwalk, 1995, p. 555.
[19] M.S. Olufsen, C.S. Peskin, W.Y. Kim, E.M. Pedersen, A. Nadim and J. Larsen, Numerical simulation and experimental validation of blood flow in arteries with structured-tree outflow conditions, *Ann. Biomed. Eng.* **28** (2000), 1281–1299.

J Med Ultrasonics (2005) 32:91–99
DOI 10.1007/s10396-005-0041-3

ORIGINAL ARTICLE

Esmeraldo dos SANTOS FILHO
Makoto YOSHIZAWA · Akira TANAKA
Yoshifumi SAIJO · Takahiro IWAMOTO

Moment-based texture segmentation of luminal contour in intravascular ultrasound images

Received: December 26, 2004 / Accepted: April 4, 2005

Abstract
Purpose. A system for luminal contour segmentation in intravascular ultrasound images is proposed.
Methods. Moment-based texture features are used for clustering of the pixels in the input image. After the clustering, morphological smoothing and a boundary detection process are applied and the final image is obtained.
Results. The proposed method was applied to 15 images from different patients, and a correlation coefficient of 0.86 was obtained between the areas of lumen automatically and manually defined.
Conclusion. Moment-based texture features together with the radial feature are powerful tools for identification of the lumen region in intravascular ultrasound images. Morphological filtering was useful for improving the segmentation results.

Keywords ultrasound · texture · image segmentation

Introduction

Cardiovascular pathologies are one of the main causes of mortality in the Western world. Atherosclerosis, a disease of the intima layer of the artery, represents the essential characteristic of arterial pathologies.[1] Atherosclerosis consists of lipids, complex carbohydrates, blood cells, fibrous tissues, and calcified deposits forming a plaque that occludes progressively the lumen of the artery. When occurring within coronary arteries, the consequences of this pathology can be dramatic, such as myocardial infarct, because the function of these arteries is to irrigate the cardiac muscle.[1]

A number of imaging modalities exist to help diagnose coronary artery diseases. Among them, X-ray coronary angiography and intravascular ultrasound (IVUS) represent the most commonly used diagnostic tools. Selective coronary angiography provides projectional X-ray images of contrast-filled coronary vessels and has been clinically used for several decades. Although it provides detailed images of the vessel lumen, it offers no information about the coronary wall. IVUS is a relatively new technique that offers image information that is complementary to that provided by angiography. It generates cross-sectional images of the lumen, plaque, and vessel wall.

Segmentation of deformable structures is a common processing problem in medical imaging. For example, coronary artery atherosclerosis severity is mainly deduced from the degree of vessel stenosis induced by the atherosclerotic plaque formation.[1–3] This is generally estimated from IVUS images by segmenting and measuring the lumen area and by referencing it to the total cross-sectional area of the vessel. With the majority of IVUS systems, this work is generally performed manually. However, as manual tracing is time-consuming, many research groups have worked on developing semiautomatic and automatic segmentation and analysis methods in IVUS images as well as angiography.[1–11]

Brusseau et al.[7] developed a fully automatic method for luminal contour segmentation in IVUS images based on an active contour that evolves until it optimally separates regions with different statistical properties. Their system used a phase-array transducer and achieved a high level of accuracy. However, no mention was made of the widely used rotating systems.

Bovenkamp et al.[8] developed an automatic multiagent-based system for luminal contour segmentation. Each agent

E. dos Santos Filho (✉)
Graduate School of Engineering, Tohoku University, 6-6-5 Aoba, Aoba-ku, Sendai 980-8579, Japan
Tel. +81-22-795-7130; Fax +81-22-263-9488
e-mail: santos@yoshizawa.ecei.tohoku.ac.jp

M. Yoshizawa
Information Synergy Center, Tohoku University, Sendai, Japan

A. Tanaka
College of Symbiotic System Science, Fukushima University, Fukushima, Japan

Y. Saijo
Institute of Development, Aging and Cancer, Tohoku University, Sendai, Japan

T. Iwamoto
Graduate School of Engineering, Tohoku University, Sendai, Japan